DISCLAIMER

Role of Water States on Water Uptake and Proton Transport in Nafion using Molecular Simulations and Bimodal Network

Gi Suk Hwang[a], Massoud Kaviany[a,*], Jeffrey T. Gostick[b], Brian Kientiz[b], Adam Z. Weber[b], Moo Hwan Kim[c]

[a] *Department of Mechanical Engineering, University of Michigan, Ann Arbor, MI 48109, USA*
[b] *Environmental Energy Technologies Division, Lawrence Berkeley National Laboratory, Berkeley, California 94720, USA*
[c] *Department of Mechanical Engineering, Pohang University of Science and Technology, Pohang, Kyungbuk 790-874, Korea*

Abstract

Using molecular simulations and a bimodal domain network, the role of water state on Nafion water uptake and water and proton transport is investigated. Although the smaller domains provide moderate transport pathways, their effectiveness remains low due to strong, resistive water molecules/domain surface interactions. The water occupancy of the larger domains yields bulk-like water, and causes the observed transition in the water uptake and significant increases in transport properties.

Keywords: water uptake, proton conductivity, water diffusivity, molecular simulations, adsorption, SAXS, bimodal network

*Corresponding author. Tel.: +1-734-936-0402; fax: +1-734-647-3170;
Email address: kaviany@umich.edu (Massoud Kaviany)

1. Introduction

Optimal water management is critical to the operation of proton-exchange-membrane fuel cells (PEMFCs)[1–3]. Key in importance is keeping the electrolyte membrane, e.g., Nafion® hydrated to ensure good proton conductivity [4], while minimizing liquid water in other PEMFC layers **for ease of gaseous fuel transport** [5, 6]. Hydration of Nafion and its transport properties are related to hydration-induced nanophase morphology, causing separation into hydrophobic-polymer-backbone and water-filled domains surrounded by hydrophilic sulfonic-acid side chains [4].

The water-filled domain size has a distribution of 1 to 1000 nm, with a mean size of $\langle L_d \rangle = 4$ nm [7–9], and this nanosize influences the water state and its transport properties. The surface energy from the domains influences the thermodynamic state of water, i.e., its chemical potential, and this directs the water adhesion towards the domain surface (adsorption). In particular, when the domain size is smaller than the intermolecular force-field distance (~ 1 nm), the surface force fields overlap each other, and this promotes water filling [10]. In addition, the domain size is much smaller than an average collision distance of the water molecules at near ambient pressure and temperature, and this significantly reduces their traveling distances (diffusion). The surface energy also impedes their motions, which in turn limits the transport, and this becomes more pronounced in the smaller domain size due to the overlapped surface force fields. So, these domain-size-dependent water states and their roles on transport properties are essential to the fundamental

understanding of hydrated Nafion and optimal fuel cell design.

Nafion hydration and transport properties have been experimentally studied for water uptake [11–17], water self diffusion [18–20], and proton conductivity [20, 21]. These observed behaviors have been explained by both continuum and atomistic modeling [22–24] with the former being focused on macroscopic, thermodynamic descriptions [25–27], and the latter on hydration-associated nanoscopic polymer dynamics [7, 8, 28–36]. Although both approaches have shown that the number of water molecules per hydrophilic, sulfonic-acid site, i.e., water content $\langle \lambda_{H_2O} \rangle$, correlate with the transport properties, their domain-size dependence has not been well explored, nor have these two approaches been correlated to each other. This lack of understanding has been in part due to limited methodologies. Macroscopic approaches have by nature relied on homogeneous treatments, and have been challenging to provide atomic-level insights on hydration and transport. Molecular approaches have also been limited to small spatial coverage for the domain-size distribution, and not extended to explain the domain-size-dependent macroscopic water uptake and its relation to transport properties. Thus, there is a critical need to bridge the two spectra. A previous study has attempted to bridge this gap using a macroscopic domain-network model, relating the adsorption-capillary water states in the Nafion domains to water uptake and proton conductivity [27]. However, this study utilized an empirical relation for the atomistic level water behavior, which is articulated here by rigorous molecular simulations. Along this line, we elucidate the roles of the domain-size-dependent water states on the water uptake and water/proton transport properties both in the individual domains and in the transport pathways

throughout the domain network. In particular, we examine the nanoscopic water states and transport in presence of the surface force fields, as continuation of our previous, domain-size-dependent water distribution **and its relation to the transport properties** [6]. For this combined nano- and macroscopic water descriptions, we propose molecular simulations combined with a bimodal domain-size network model.

2. Proposed Bimodal Network Model

2.1. Bimodal Domain Size

The microstructure of hydrated Nafion including its connectivity and hydrophilic-site distribution, is crucial to the water states, transport properties, and mechanical properties. Much effort has been made over last few decades to characterize the structure underlying its unique, high proton conductivity, however, due to its low crystallinity and complex chemical composition, an exact structure is still contentious [4], which will return to at the end of this section. Since the primary focus here is the water state and the transport properties, an idealized bimodal-domain distribution network for hydrated Nafion is proposed using uniform density of the hydrophilic sites. Such a construct is guided by our small-angle X-ray scattering (SAXS) measurement, the reported domain-size distribution measurement [9], and the available bimodal cluster network model [7, 8]. As shown in Figure 1(a), the large domains are represented by the mean domain size, 4 nm, while the small ones are determined by the Debye screening length δ_{D}, (the distance

over which charge carriers screen out the surface electric field) [37],

$$\delta_{\mathrm{D}} = \left(\frac{\epsilon_{\mathrm{o}}\epsilon_{\mathrm{r}}k_{\mathrm{B}}T}{4\pi e^2 \sum_i n_i z_{e,i}^2}\right)^{1/2}, \tag{1}$$

where ϵ_{o} and ϵ_r are the free-space electric and relative permittivities, respectively, k_{B} is the Boltzmann constant, T is the temperature, and n_i and $z_{e,i}$ are the number density and the number of conduction electrons per contributing ions, respectively. $\delta_{\mathrm{D}} = 0.23$ nm is predicted using an equivalent weight (EW) of 1100 g/mol, a density of 2 g/cm^3 [38], and the number densities of two types of ions, i.e., the sulfonic acid and hydronium. The calculated Debye length is the hard sphere diameter, $d_{\mathrm{H_2O}} = 0.3$ nm, meaning that the effective interaction length is one layer of adsorbed water. This length is also consistent with the predictions using the Pekar-Marcus relation [39] and the mean field Poisson-Boltzmann theory [40]. Using 1.5 adsorbed-water layer and the two confining domain surfaces, a 1 nm nanogap (domain size) is set as the small domain size.

The bimodal domain sizes lead to bimodal water filling (complete and partial water occupation), which results in selective transport pathways through the water-filled domains in a network, as shown in Figure 1(a). During the water uptake, thermodynamic equilibria among neighboring domains in the network require that the connected domains have the same chemical potential. This condition results in first filling of the smaller domains due to their overlapping surface force fields, and then filling of the larger domains because of weaker surface interactions. The weak surface interactions mean more of a bulk-like water phase since the subse-

quent adsorbed-water layers are formed outside the Debye screening length. This finding has also been reported in previous studies [23, 41], and this study further articulates the nanoscale water behavior using molecular simulations.

The microstructure of hydrated Nafion has been primarily examined to understand the unique structure that yields its high proton conductivity. The primary models are the bimodal cluster-network [7, 8], the structural-inversion [42], the sandwich-like [30], the percolation-channel [31], and the parallel-channels models [35]. It has been known that the mean characteristic size of the microstructure is 4 nm and its size increases with water activity (hydration). The graphical descriptions of these models are shown in Figures 1(b)-(f), with water activity as a variable.

The bimodal, cluster-network model, Figure 1(b), proposes two characteristic cluster-domain sizes, such that the primary clusters are connected by the secondary transport channels, which evolve with water activity and become the larger percolated transport channels. Although this model has been the most popular and is similar to ours, it does not contain the viable molecular descriptions and cannot support the SAXS measurement [35]. In the structural-inversion model, Figure 1(c), the swelling and dissolution processes have been phenomenologically described, showing a possible structural-inversion between the water and the polymer structure at high water activity, but no quantitative study has been done to date. In the sandwich-like model, Figure 1(d), a simple nanogap has been proposed to predict the SAXS experimental

results by quantifying the hydration-dependent structural change (swelling), but the water states and the resulting water/proton transport have not been addressed. In the percolation model, Figure 1(e), **the phenomenological descriptions on water state and its transport have highlighted the Schröder paradox which has been an inexplainable, larger water-uptake increase ($\langle\lambda_{H_2O}\rangle$ = 14 and 22) between fully vapor-equilibrated and liquid-equilibrated membranes at the same chemical potential, and attempts have been made to relate it to the capillary percolation.** However, capillary percolation occurs at lower hydration $\langle\lambda_{H_2O}\rangle = 5$ or 6, due to the strong surface interactions [6]. In the long parallel-channel model, Figure 1(f), the proposed, long, cylindrical-domain network **including semicrystal structures** has best fitted the SAXS results, but the model has not been related to the nanoscopic descriptions on water states and the transport properties. **It has also been found that the microstructure changes with hydration, temperature, and pretreatment, meaning that various morphologies may exist under different conditions [43]. However, the structure-related, nanoscale-water behaviors have not been addressed in any of the existing Nafion morphology models.**

The key outcomes of this study rely on the nanoscale-water states and dynamics in the domains, and the resulting transport pathways in the network. These phenomena are related to the strength of the water/surface interactions which are affected by the microstructure. The spherical [7, 8] and cylindrical [35] structures increase the specific surface area (total surface area per unit

volume) compared to our nanogap. The increased surface area reduces the site density per unit surface area, and in turn weakens the surface force fields. This is expected to result in decreased water adsorption, reluctant water filling, and increased free-water motion. On the other hand, the spherical and/or cylindrical structures increase the surface curvature where the surface force fields overlap, which in turn strengthens them. The stronger fields lead to increased adsorption, favorable water filling (by reducing the capillary meniscus in the Kelvin-Cohan relation [44]), and hindered water motion. The two geometric effects above result in an expected, negligible net impact. It is implied that the nanoscale-water descriptions in our nanogap structure represent the water states and transport properties of hydrated Nafion without a significant loss of generality.

2.2. SAXS Measurement

The bimodal domain size are further informed by our analysis of SAXS measurements. Nafion 117 specimens were tested using SAXS at the Advanced Light Source at the Lawrence Berkeley National Laboratory, with a X-ray wavelength of 1.239 Å. In preparation for the tests, the samples were boiled for one hour in a 1M H_2SO_4 solution to remove any ionic impurities and to ensure a fully protonated state. Samples were mounted in a sealed sample holder such that they were suspended above a pool of pure water, saturated LiCl solution, or desiccant, and allowed to equilibrate over 4 hours with data taken every 5 minutes. The sample holder is shown in Figure 2(a). Kapton-covered holes through the holder allowed unimpeded X-ray access

to the hanging sample while maintaining a sealed environment. Background spectra were collected for each test and assumed to apply for the duration of the drying data gathering. The measured scattering X-ray intensities were subtracted from the background scattering, and then were normalized by the transmitted intensity. **Figure 2(b) shows the scattered intensities (arbitrary unit) with respect to the scattering wave vector (q = 0.05 to 0.3 Å^{-1}) at water activities of a_{H_2O} = 0, 0.11, and 1.0. One (ionomer) peak is observed for dry Nafion (a_{H_2O} = 0), and this shifts to lower q with an increase in water activity (q = 0.185 to 0.15 Å^{-1}). This is primarily related to the water-filled, domain size growth by swelling (the domain size change of 3.3 to 4.2 nm) [4, 7]. Indeed, the intensity at the low q (matrix knee) is related to the semicrystalline structures from long polymer matrix chains, which is important to its mechanical properties, while the intensity at the large q (Prod's law) represents the domain surface area [35, 45]. In addition, we note that the water morphologies in the domains (partial/complete water occupation) can be another source of the peak shift, although the thin, adsorbed-water layers are the secondary X-ray scatters.**

To model this, cubical domains are constructed in a network, as shown in Figure 2(c). **Each domain** includes polymer matrix, an adsorbed-water layer, and a water-fillable layer **as sources of the X-ray scattering**. The last layer represents the potential, water-filling layer at high water activity and is not expected to influence significantly the water transport due to the absence of surface interaction with water. Practically, this water-fillable layer

is occupied by the polymer matrix, where it swells/shrinks with hydration. However, we use idealized, rigid domains, along with the water-filling layer, for feasible molecular simulations. The rigorous descriptions associated with the adsorbed/water-fillable requires modifications of the existing sandwich-like model [30], and after adding these the layers, we have

$$I^*(q) = \alpha \int_0^1 \frac{2}{\pi} \int_0^{\pi/2} S^2(L_X, \phi, a) \mathrm{d}\phi [\Delta n_{e,p}(S(L_Z, a) - S(L_{Z,d}, a)) + \Delta n_{e,ad,\mathrm{H_2O}}(S(L_{Z,d}, a) - S(L_{Z,wf}, a)) + \Delta n_{e,g,\mathrm{H_2O}} S(L_{Z,wf}, a)]^2 \mathrm{d}a, \quad (2)$$

where

$$S^2(L_X, \phi, a) = \frac{\sin[0.5qL_X \cos(\phi)(1-a^2)^{1/2}]}{0.5qL_X \cos(\phi)(1-a^2)^{1/2}} \frac{\sin[0.5qL_X \sin(\phi)(1-a^2)^{1/2}]}{0.5qL_X \sin(\phi)(1-a^2)^{1/2}} L_X^2, \quad (3)$$

$$S(L_Z, \phi, a) = \frac{\sin(0.5qL_Z a)}{0.5qL_Z a} L_Z, \quad a = \cos(\phi), \quad (4)$$

where S is the form factor, Δn_e is the electron density variation, $L_{Z,d}$ is the domain size, $L_{Z,wf}$ is the water-fillable layer thickness, L_X is the lateral domain size, and α is the scaling factor. In the network, **the individual domains are randomly rotated, and** hydrated Nafion has a water-filled domain volume ratio, $\epsilon = 0.4$ [9, 27, 46]. Using $L_X = L_Z = 6$ nm guided by our experimental result at $a_{\mathrm{H_2O}} = 1$ (Table 1), the domain population ratios are 0.53 and 0.47 and the domain volume ratios are 0.22 and 0.78, for $L_{Z,d} = 1$ and 4 nm, respectively, as summarized in Table 2. Using the bimodal domain size, the predicted $L_{Z,wf}$ (which will be predicted using molecular simulations in the next section), and the domain population ratio, the predicted peaks for $a_{\mathrm{H_2O}} = 0$, 0.11, and 1 show reasonable agreements with the measured data, particularly near $q > 0.125$ Å as shown in Figure 2(b). The peak in q (characteristic length) is related to an average distance associated with the

L_X or L_Z, $L_{Z,d}$ and $L_{Z,wf}$, and the domain-size distribution. The predictions using the parameters given in Table 1 agree with the measured peak at $q \sim$ 0.15 to 0.185 Å^{-1}.

2.3. Bimodal Water Filling

The bimodal water filing is related to the bimodal strength of the water/surface interactions, and it is analyzed by the isosteric heat of adsorption [47]. Using Eq. (A.1), the heat of adsorption is calculated as a function of the number of adsorbed-water layers, $N_{ad,\mathrm{H_2O}}$, for the two domain sizes, as shown in Figure 3. The total adsorbed-water-layer thickness, $\delta_{\mathrm{H_2O},ad}$ (summation of two layers from top and bottom) using $d_{\mathrm{H_2O}} = 0.3$ nm is also shown at the top x axis. The Debye screening length is also marked **to show water-behavior changes by the surface force fields**. As the adsorbed-water layer grows beyond the Debye length, the heat of adsorption decreases towards the bulk value, i.e., the heat of evaporation (46 kJ/mol at $T = 300$ K for MSPC/E water model [48]), since the surface interactions are significantly screened. In the small domains, the heat of adsorption is nearly doubled for small adsorption, and is still higher compared to the bulk heat of evaporation at large adsorption. In contrast, in the large domain it is only 15% higher for the small adsorption and then becomes nearly the same as the bulk. This indicates that the small domains significantly change water behavior due to strong interactions, whereas the large domains lead to bulk-like water due to no significant surface interactions. **In addition, an increase in sulfonic-acid-site density, $n(\mathrm{SO_3^-}) = 1.75$ to 2.5 nm^{-2}, strengthens the water interactions with the surfaces. This change is more pronounced in the larger domains because the**

smaller domains already have strong surface forces (overlapping force fields). This result implies that the water-state changes with respect to the hydrophilic-site concentration (or equivalent weight) are more significant in the larger domains than those in the smaller domains. The strength of the surface forces is also related to the water filling, which will be discussed further below.

3. Water Uptake

The bimodal-size and water-filling model succeeds in explaining water uptake and its significant increase near high water activities. The water states of each domain size are explored using the grand canonical molecular dynamics-Monte Carlo (GCMD-MC) simulation, as described in Appendix A, and the results are integrated over the entire network through the prescribed chemical potential (water activity). One of the important factors for the water states in the domains is the surface sulfonic-acid density $n(SO_3^-)$. The reported values have a range of 0.51 to 3.3 nm^{-2} as summarized in Table 3 [8, 9, 36, 42]. Here, using $n(SO_3^-)$ = 1.5, 1.75, and 2.5 nm^{-2}, the number of water molecules per volume of each domain, n_{H_2O}, are shown in Figures 4(a) and (b) at T = 300 K for $L_{Z,d}$ = 1 and 4 nm, respectively. **Note that n_{H_2O} = 37 nm^{-3} represents complete water filling**. At low activities, there is only adsorbed-water layer without water filling, and its thickness grows as the activity increases. At the threshold activities, the domain begins to fill completely. The threshold activity increase in the large domains due to the weaker overlapping surface forces. However, no significant variation in the threshold is found in the small domains because of the

strongly overlapped surface force fields. These predicted, nanoscale water states are validated by the available modified BET theory, the Kelvin-Cohan (K-C) relation [27, 49], and the Saam-Cole (S-C) transition theory (using the homogeneous water-water effective potential for the water-surface wall interactions beyond the Debye length [6, 10]). Although these theories reasonably predict the water filling of the large domains, the prediction using Kelvin-Cohan relation is close to the GCMD-MC results with a large sulfonic-acid-site density i.e., $n(SO_3^-) = 2.5$ nm^{-2}. The Saam-Cole theory predicts a delayed threshold. This delay is due to the large (bulk) surface tension, while the effective water-water intermolecular potential tends to be weaker than the surface-water interaction.

The sulfonic-acid-site density influences the adsorption and water filling. Higher surface energy or hydrophilic-site density (strong surface force, $n(SO_3^-) = 2.5$ nm^{-2}) increases adsorption, and the water filling occurs at lower activity. However, the lower density (weak surface force, 1.5 nm^{-2}) decreases adsorption, and the filling does not occur at $a_{H_2O} = 1$, indicating that the surface is extremely hydrophobic and the expected water uptake with the fully vapor-equilibrated reservoir is significantly lower than the experimental results. Thus, we choose $n(SO_3^-) = 1.75$ nm^{-2} as the characteristic Nafion sulfonic-acid-site density for a good agreement with the available experimental water uptake data as well as the available water diffusivity and proton conductivity as shown below.

In general, the adsorbed water in Nafion is presented as water content defined by the number of water molecules per sulfonic-acid site [21]. To predict the water content, $\langle \lambda_{H_2O} \rangle$, the total adsorbed water amount in the network

is calculated by integrating the water states in the individual domains over the two domain sizes, as given by

$$\langle \lambda_{H_2O} \rangle = \frac{\sum_i n_{H_2O,ad} V_{L_{Z,d,i}}}{N(SO_3^-)}, \tag{5}$$

where $n_{H_2O,ad}$ is the number density of the adsorbed water in the individual domain, $V_{L_{Z,d,i}}$ is the domain volume for each, and $N(SO_3^-)$ is the total number of sulfonic-acid sites. The predicted water content is shown in Figure 4(c). It is small at low water activity, and increases with increasing water activity. At the threshold water activities, $a_{H_2O} = 0.1$ and 0.95, the water uptake significantly increases, which is related to the filling of the large domains. The first transition is caused by filling the smaller domains, $L_{Z,d} = 1$ nm, and the second is more pronounced by fully hydrating the larger domains, $L_{Z,d} = 4$ nm, due to a significant domain volume ratio. This agrees with the experimental result [21], especially at the large water content, while overpredicting at low water activities. The assumption of a rigid domain structure based on the fully hydrated Nafion causes the discrepancy at the low water activities. In addition, our model does not include hydrodynamic resistance among domains, or interfacial rearrangement and/or resistance [17, 50, 51], which also help to explain this overprediction.

4. Water Self Diffusion

Water self diffusion occurs through **the completely water-filled transport pathways [Figure 1(a)]. Hydration controls not only nanoscale water motions (local diffusivity) in the individual domains, but also**

the transport channel connectivity (or tortuosity of transport pathways). In the individual domains, the diffusivities, D_{H_2O} are calculated using **the molecular simulations** and the Green-Kubo autocorrelation, Eq. (A.2), at $T = 300$ K as a function of a_{H_2O}, and the results are reported in Table 4. Next, the effective diffusivity $\langle D_{H_2O} \rangle$ is calculated using 30×30 domains in the 2-D bimodal network as depicted in Figure 1(a), and the results are shown in Figure 5(a) as a function of the predicted water content [Figure 4(c)]. No calculation size effect is found up to 100×100 domains. Calculation details have been given previously [52].

At $\langle \lambda_{H_2O} \rangle \sim 2$ ($a_{H_2O} \sim 0.05$), the effective diffusivity is significantly low compared to that in bulk liquid water **because the movement of water molecules are significantly hindered by the strong surface force fields (most of water molecules are within the Debye screening length, Table 4). The transport pathways are also significantly limited by the partially-filled domain network.** At $\langle \lambda_{H_2O} \rangle \sim 4$ ($a_{H_2O} \sim 0.1$), **the effective diffusivity begins to increase primarily by approaching the bulk-like diffusivity in the water-filled small domains and by increasing the transport pathways.** At $\langle \lambda_{H_2O} \rangle \sim 5$ ($a_{H_2O} \sim 0.3$), the adsorbed layers in large domains grow beyond the screening length, and for $\langle \lambda_{H_2O} \rangle > 5$, further filling of the large domains **increases the effective diffusivity.** These results are in good agreement with experiments [18] and available MD results [53, 54], and our multiscale approach better predicts compared to the full atomistic simulations [53, 54], **where the limited simulation size may not represent the domain-size-dependent water transport.** With a consideration of hydration-dependent Nafion morphol-

ogy **(swelling), i.e., reduced domain sizes at low water activity**, the water uptake is expected to decrease especially at the low water content, and this consideration results in better agreement with the experimental data. For validation, our MD-predicted bulk-liquid diffusivity at $T = 298$ K is in excellent agreement with existing data [55].

The role of the water-filled transport channels on the effective water diffusivity is elucidated by examining the pathway tortuosity. In permeable media, the effective self diffusivity $\langle D_{H_2O} \rangle$ is related to the bulk diffusivity D_{H_2O}, permeable domain volume ratio ϵ, and tortuosity L_t^*, as given as [56]

$$\langle D_{H_2O} \rangle = \frac{D_{H_2O} \epsilon}{L_t^*}. \tag{6}$$

The tortuosity is calculated using the homogeneous, bulk diffusivity for all the bimodal domains with a constant domain volume ratio of $\epsilon = 0.4$ as a function of water content. **Note that $L_t^* = 1$ represents a full transport-network connectivity, which occurs at high water activity.** Using the bulk diffusivity for all the domains, it predicts only the tortuosity without considering the surface-force-induced transport, as shown in Figure 5(b). The tortuosity decreases with increasing water content, **showing that** the smaller domains form minor transport channels at low water content, and the larger domains provide major domain connectivity. Using **the molecular-simulation-calculated** diffusivity (surface-force-hindered diffusivity, Table 4), the tortuosity predicts 30 to 70% lower than the above predictions (without considering the surface-force hindrance). This resistance is caused by the transport impedance from the domain-surface interactions. **Note that the resistance difference is minimized where the water fillings occur,**

indicating that the complete water occupation yields the bulk-like water behavior.

5. Proton Transport

In bulk liquid water, protons transfer via Grotthuss (or hopping) diffusion **and translational diffusion (or vehicle motion). The former is the dominant mechanism, where** a proton effectively hops over a hydrogen-bond network of water molecules using fast bond-breaking and making steps [57–61]. In the **hydrated-**Nafion domain network, such transport is **hindered by the strong surface force fields, and the effective proton conductivity decreases. Since the force fields are significant within the Debye length,** no significant Grotthuss diffusion is considered, and the surface-force hindered translational hydronium diffusion is included (Table 5). Using the Nernst-Einstein relation [25, 26], we have

$$\sigma_{\mathrm{H^+}} = \frac{e_{\mathrm{H^+}}^2}{k_{\mathrm{B}}T}(n_{\mathrm{H_3O^+}} D_{\mathrm{H_3O^+},D} + n_{\mathrm{H^+}} D_{\mathrm{H^+,G}}), \tag{7}$$

where $e_{\mathrm{H^+}}$ is the proton charge, $n_{\mathrm{H^+}}$ is the number density of protons for Grotthuss diffusion, $n_{\mathrm{H_3O^+}}$ is the number density of hydronium for translational diffusion, $D_{\mathrm{H^+,G}}$ is the Grotthuss diffusivity, and $D_{\mathrm{H_3O^+},D}$ is the translational diffusivity. $D_{\mathrm{H_3O^+,D}}$ is calculated using MD-simulated, 8 to 18 hydroniums, and the Green-Kubo autocorrelation relation Eq. (A.2), as presented in Table 5. The Grotthuss diffusivity is calculated using the available relaxation time for water-molecule rotations [25, 26, 62]. At $T = 300$ K, $D_{\mathrm{H^+,G}} = 7{\times}10^{-9}$ m^2/s, using $D_{\mathrm{H^+,G}} = d_{\mathrm{O\text{-}O}}^2/6\tau_{\mathrm{D}}$, and relaxation time of $\tau_{\mathrm{D}} = 1.5$ ps, and O-O distance of 0.255 nm in $\mathrm{H_9O_4^+}$ [62]. For the total proton number density,

equivalent weight of 1100 g/mol, and density of 2 g/cm^3 are used, while for the bulk-like domains, $n_{H^+}/(n_{H^+}+n_{H_3O^+}) = 0.5$ is assumed. We note that this population density ratio is so far not confirmed, even with the recent microscopic analyses and *ab initio*-molecular-dynamics simulations [57–61].

Similarly, using the 2-D, 30×30 domain network and the Kirchhoff law at the domain junctions [27], the effective conductivity $\langle\sigma_{H^+}\rangle$ is calculated as a function of the water content $\langle\lambda_{H_2O}\rangle$, as shown in Figure 6(a).

In Figure 6(a), at $\langle\lambda_{H_2O}\rangle < 2$, proton conductivity is negligibly small, because the adsorbed water is mainly within the screening length. As the activity increases, the small domains readily fill, and at $\langle\lambda_{H_2O}\rangle \sim 4$ the proton conductivity significantly increases through bulk-like proton diffusion and hopping **as marked by the onset of hopping at $L_{Z,d} = 1$ nm.** However, in the large domains, the conductivity is still hindered, which in turn causes no significant proton conductivity increase. At $\langle\lambda_{H_2O}\rangle \sim 8$, the adsorbed water layers in the large domains grow beyond the screening length, and the bulk-like diffusion and hopping result in significant enhancement **as indicated by the onset of hopping at $L_{Z,d} = 4$ nm. The detailed discussions on the water-filling related transport property transition are found in our previous work [6].** At high activities, water filling occurs and leads to the maximum conductivity. The diffusive proton conductivity is also shown, indicating that its contribution is only nearly one third. For comparison, a previously reported MD result is also shown, and it can be seen that it underestimates the proton conductivity **without addressing the significant enhancement at $\langle\lambda_{H_2O}\rangle \sim 5$ since it has not properly considered the domain-size-dependent transport proper-**

ties [63]. Similar to Figure 5(b), the normalized effective conductivity is shown in Figure 6(b). At low water content, $\langle \lambda_{H_2O} \rangle \sim 2$, the proton conductivity is a minimum due to the large hindrance from the ionic surface although there are water pathways through the smaller domains **(the pathways are small as indicated by the small domain filling).** At $\langle \lambda_{H_2O} \rangle \sim 8$, the water molecules are outside the Debye length especially in the larger domains, and the conductivity increases significantly.

6. Conclusions

Using the proposed molecular simulations combined with the bimodal-domain-network model, we explained the role of water states on the water uptake and water and proton transport in Nafion, while addressing both nano- and macroscopic water behavior. The water states, i.e., adsorption and water filling, are domain-size dependent in the individual domains, and the water occupation forms selective transport pathways in the network. Although the smaller domains readily fill water and form network pathways, the strong overlapping surface forces retard the water and proton transport. However, in the larger domains, the water filling is delayed and their water occupation significantly increases both the water uptake and water and proton transport properties since the water molecules are beyond the Debye transport impeding length. Although idealized, this model provides nanoscopic insights on water states and the resulting transport, while addressing the macroscopic water description. The domain-size-dependent water descriptions contribute to complimentary understanding of the role of water states on water/proton transport in ion-conducting polymers. In addition, our grand canonical

molecular dynamics - Monte Carlo (GCMD-MC) approach allows for predictions of the water content as a function of water activity, something that is challenging for conventional MD simulations. This methodology allows not only a direct comparison with water-uptake experiments, but also allows for extending the treatment to intrinsic, temperature-dependent water uptake with inclusion of the flexibility of the polymer matrix.

Acknowledgements

We are thankful for the sponsorship of Global Partnership Program (Ministry of Science and Technology, South Korea), assistance by Drs. Alexander Hexemer and Cheng Wang (Lawrence Berkeley National Laboratory) on the SAXS measurements, and discussions with Professor Reinhard Hentschke (University of Wuppertal, Germany) on the GCMD-MC simulation. This work was partially supported by the Assistant Secretary for Energy Efficiency and Renewable Energy, Office of Fuel Cell Technologies, and the Director, Office of Science, Office of Basic Energy Sciences (for support of the Advanced Light Source), of the U.S. Department of Energy under contract number DE-AC02-05CH11231.

Appendix A. GCMD-MC

To simulate physiochemical properties such as water adsorption (static quantity) and water/proton transport (dynamic characteristics), we use a combination approach, i.e., GCMD-MC simulation which allows controlling the number of water molecules by the Metropolis algorithm during the NVT ensemble molecular dynamics. The algorithm/calculation details are given

in the previous work [64]. The Nafion domain is represented as two infinite, parallel slabs (using periodic boundary conditions in the x and y directions) separated by a physical width, L_z [33], as shown in Figure 2(c). We assume that the surfaces are uncorrugated, stationary, and rigid (no swelling). The hydrophobic surface is modeled by 1-D Lennard-Jones potential, whereas the hydrophilic sites are represented by SO_3^- only [33]. The number of sites per domain are 8 to 18 for $T = 300$ K, and the lateral domain sizes are adjusted to represent the desired surface site density of $n(SO_3^-) = 1.5$ to 2.5 nm^{-2}. The dominant source of the water-surface interactions is the electrostatic force between the hydrophilic, ionized sulfonic-acid side chain and the water molecules. Although there are intermolecular interactions between hydrophobic polymer backbone and water molecules, those are in general significantly weak interactions compared to the ones with the hydrophilic sites. So, it is expected that modeling of the hydrophobic matrix would not significantly change water adsorption, and it is simplified using the available interactions [33]. While we understand that the true morphology of Nafion is hydration dependent with the various domain sizes being primarily a force balance between the electrostatic interactions and polymer-chain elongation [65, 66], we use the vapor-equilibrated structure under all hydration cases to make the simulations tenable. Although the domain size has a range of 1 to 1000 nm in radius [9], it is modeled as bimodal sizes. This approach gives minimal loss of fidelity in the treatment of the water uptake and transport properties.

For the water molecules, the modified simple polarization charge extended (MSPC/E) water is used [48]. This water potential is superior to SPC,

and SPC/E which is for vapor-liquid equilibria at $T = 300.15$ to 582.28 K, relevant to adsorption. An equal number of hydroniums are added to neutralize electrically the sulfonic-acid system using an available potential [67]. The chemical potential and the vapor pressure are calculated using a virial expansion [64, 68], and the second-order virial coefficient [69]. The leapfrog Verlet algorithm [70] is used to solve the Newton equation, the SHAKE algorithm is used for the rigid molecules [71], and the temperature is controlled by a Brendsen thermostat [72]. The long-range electrostatic force is calculated by the pairwise additive method [73], where the damping coefficient, $\alpha = 0.2$ Å^{-1}, and cutoff $r_c = 1.2$ nm are used. The simulation temperatures are $T = 298$ K. The time step $\Delta t = 0.5$ fs is used for a time integration, and the total simulation time is 1.5 to 3 ns, until there is no significant change in the water-molecule population, <5% for 1 ns. This method is validated by testing bulk vapor/liquid water density at $T = 300$ K [48]. The resulting water densities (or pressures) agree well with the available simulation results [48].

The isosteric heat of adsorption is calculated using [74]

$$\Delta h_{lg,ad} = -\frac{\langle \varphi N \rangle - \langle \varphi \rangle \langle N \rangle}{\langle N^2 \rangle - \langle N \rangle^2} + k_{\mathrm{B}} T, \tag{A.1}$$

where φ is the system potential energy and N is the number of particle in the nanodomain.

The self-diffusion coefficient D_i for species i in the individual domain is calculated using the Green-Kubo autocorrelation relation given as [75],

$$D_i = \lim_{\tau \to \infty} \int_0^{\tau} \mathrm{d}t \langle u_i(t) u_i(0) \rangle, \tag{A.2}$$

where i is either water or hydronium, t and τ are times, $u_i(t)$ is the velocity

of the species i from MD results. Since the species i in the nanogap diffuses only in x- and y-directions, x- and y-direction velocity profiles are used for the average diffusivity, and $\tau = 100$ ps is used.

References

[1] O'Hayre R, Cha S, Prinz F, Colella W. Fuel Cell Fundamentals. John Wiley & Sons, Inc., New York; 2005.

[2] Barbir F. PEM Fuel Cells. Elsevier Academic Press; 2005.

[3] Eikerling M, Kornyshev A, Kucernak A. Water in polymer electrolyte fuel cells: Friend or foe? Phys Today Oct. 2006;59:38–44.

[4] Mauritz K, Moore R. State of understanding of Nafion. Chem Rev 2004;104:4535–85.

[5] Weber A, Newman J. Effects of microporous layers in polymer electrolyte fuel cells. J Eelectrochem Soc 2005;152(4):A677–88.

[6] Hwang G, Kaviany M, Nam J, Kim M, Son S. Pore-water morphological transitions in polymer electrolyte of a fuel cell. J Electrochem Soc 2009;156:B1192–200.

[7] Gierke T, Munn G, Wilson F. The morphology in Nafion perfluorinated membrane products, as determined by wide- and small-angle X-ray studies. J Polym Sci 1981;19(11):1687–704.

[8] Hsu W, Gierke T. Ion transport and clustering in Nafion perfluorinated membranes. J Membrane Sci 1983;13:307–26.

[9] Divisek J, Eikerling M, Mazin V, Schmitz H, Stimming U, Volfkovich Y. A study of capillary porous structure and sorption properties of Nafion proton-exchange membranes swollen in water. J Eelectrochem Soc 1998;145(8):2677–83.

[10] Saam W, Cole M. Excitation and thermodynamics for liquid-helium films. Phys Rev B 1975;11:1086–105.

[11] Zawodzinski T, Springer T, Davey J, R.Jestel , Lopez C, Valerio J, et al. A comparative study of water uptake by and transport through ionomeric fuel cell membranes. J Eelectrochem Soc 1993;140(7):1981–5.

[12] Hinatsu J, Mizuhata M, Takenaka H. Water uptake of perfluorosulfonic acid membranes from liquid water and water vapor. J Eelectrochem Soc 1994;141(6):1493–8.

[13] Broka K, Ekdunge P. Oxygen and hydrogen permeation properties and water uptake of Nfion 117 membrane and recast film for PEM fuel cell. J Appl Electrochem 1997;27(2):117–23.

[14] Guo X, Fang J, Tanaka K, Kita H, Okamoto K. Synthesis and properties of novel sulfonated polyimides from 2,2'-bis(4-aminophenoxy)biphenyl-5,5'-disulfonic acid. J Polym Sci, Part A: Polym Chem 2004;42(6):1432–40.

[15] Onishi L, Prausnitz J, Newman J. Water-Nafion equilibria. absence of schroeder's paradox. J Phys Chem B 2007;111:10166–73.

[16] Gebel G, Diat O, Escribano S, Mosdale R. Water profile determination

in a running PEMFC by small-angle neutron scattering. J Power Sources 2008;179:132–9.

[17] Mukherjee PP, Mukundan R, Spendelow JS, Davey JR, Borup R, Hussey DS, et al. High resolution neutron imaging of water in the polymer electrolyte fuel cell membrane. ECS Transactions 2009;25(1):505–12.

[18] Zawodzinski T, Jr. , Neeman M, Sillerud L, Gottesfeld S. Determination of water diffusion coefficients in perfluorosulfonate ionomeric membranes. J Phys Chem 1991;95:6040–4.

[19] Motupally S, Becker A, Weidner J. Diffusion of water in Nafion 115 membranes. J Electrochem Soc 2000;147:3171–7.

[20] Ye X, Wang C. Measurement of water transport properties through membrane-electrode assemblies, I. Membranes. J Eelectrochem Soc 2007;154(7):B676–82.

[21] Zawodzinski T, Derouin C, Radzinski S, Sherman R, Smith V, Springer T, et al. Water uptake by and transport through Nafion 117 membranes. J Eelectrochem Soc 1993;140(4):1041–7.

[22] Weber A, Newman J. Modeling transport in polymer-electrolyte fuel cells. Chem Rev 2004;104:4679–726.

[23] Kreuer KD, Paddison S, Spohr E, Schuster M. Transport in proton conductors for fuel-cell applications: Simulations, elementary reactions, and phenomenology. Chem Rev 2004;104:4637–78.

[24] Kim Y, Pivovar B. Mass-based parameters for conductivity analysis of sulfonated polymers. Annu Rev Chem Biomol Eng 2010;1:123–48.

[25] Choi P, Datta R. Sorption in proton-exchange membranes: An explanation of Schroeder's paradox. J Eelectrochem Soc 2003;150(12):E601–7.

[26] Choi P, Jalani N, Datta R. Thermodynamics and proton transport in Nafion II. Proton diffusion mechanisms and conductivity. J Eelectrochem Soc 2005;152(3):E123–30.

[27] Costamagna P, Grosso S, Felice RD. Percolative model of proton conductivity of Nafion membranes. J Power Sources 2008;178(2):537–46.

[28] Eikerling M, Kornyshev A, Stimming U. Electrophysical properties of polymer electrolyte membranes: A random network model. J Phys Chem B 1997;101:10807–20.

[29] Cornet N, Beaudoing G, Gebel G. Influence of the structure of sulfonated polyimide membranes on transport properties. Sep Purif Technol 2001;22-23:681–7.

[30] Haubold HG, Vad T, Jungbluth H, Hiller P. Nano structure of Nafion: a SAXS study. J Phys Chem B 2001;46:1559–63.

[31] Weber A, Newman J. Transport in polymer-electrolyte membranes, I. Physical model. J Eelectrochem Soc 2003;150(7):A1008–15.

[32] Kreuer K, Paddison S, Spohr E, Schuster M. Transport in proton conductors for fuel-cell applications: Simulations, elementary reactions, and phenomenology. Chem Rev 2004;104:4637–78.

[33] Sphor E. Molecular dynamics simulations of proton transfer in a model Nafion pore. Mol Simulat 2004;30:107–15.

[34] Wescott J, Qi Y, Subramanian L, Capehart T. Mesoscale simulation of morphology in hydrated perfluorosulfonic acid membranes. J Chem Phys 2006;124:134702–1–14.

[35] Schmidt-Rohr K, Chen Q. Parallel cylindrical water nanochannels in Nafion fuel-cell membranes. Nature Mat 2008;7:75–83.

[36] Malek K, Eikerling M, Wang Q, Liu Z, Otsuka S, Akizuki K, et al. Nanophase segregation and water dynamics in hydrated Nafion: molecular modeling and experimental validation. J Chem Phys 2008;129:204702–1–10.

[37] Robinson R, Stokes R. Electrolyte Solutions, 2nd Ed. Dover Publications, New York; 2002.

[38] Weber A, Newman J. Transport in polymer-electrolyte membranes, III. Model validation in a simple fuel-cell model. J Eelectrochem Soc 2004;151(2):A326–39.

[39] Eikerling M, Kornyshev A, Sphor E. Proton-conducting polymer electrolyte membranes: Water and structure in charge. Adv Polym Sci 2008;215:15–54.

[40] Eikerling M, Kornyshev A. J Electroanal Chem 2001;502:1–14.

[41] Kreuer K. Fast proton conductivity: A phenomenon between the solid and the liquid state? Solid State Ionics 1997;94:55–62.

[42] Gebel G. Structural evolution of water swollen perfluorosulfonated ionomers from dry membrane to solution. Polymer 2000;41:5829–38.

[43] Majsztrik P, Bocarsly A, Benziger J. Viscoelastic response of Nafion. Effects of temperature and hydration on tensile creep. Macromolecules 2008;41:9849–62.

[44] Park M, Downing K, Jackson A, Gomez E, Minor A, Cookson D, et al. Increased water retention in polymer electrolyte membranes at elevated temperatures assisted by capillary condensation. Nano Lett 2007;7:3547–52.

[45] Gebel G, Diat O. Neutron and X-ray scattering: Suitable tools for studying ionomer membranes. Fuel Cells 2005;5:261–76.

[46] Weber A, Hickner M. Modeling and high-resolution-imaging studies of water-content profiles in a polymer-electrolyte-fuel-cell membrane-electrode assembly. Electrochim Acta 2008;53(26):7668–74.

[47] Puibasset J, Pellenq R. Water adsorption in disordered mesoporous silica (vycor) at 300 k and 650 k: A grand canonical monte carlo simulation study of hysteresis. J Chem Phys 2005;122:094704–1–10.

[48] Coulougouris G, Economou I, Theodorou D. Engineering a molecular model for water phase equilibrium over a wide temperature range. J Phys Chem B 1998;102:1029–35.

[49] Do D. Adsorption Analysis: Equilibria and Kinetics. Imperial College Press,; 1998.

[50] Monroe C, Romero T, Mérida W, Eikerling M. A vaporization-exchange model for water sorption and flux in Nafion. J Membr Sci 2008;324:1–6.

[51] Kienitz B, Yamada H, Nonoyama N, Weber A. Interfacial water-transport effects in proton-exchange membranes. J Fuel Cell Sci Technol 2011;8:011013–9.

[52] J.H. Nam , Kaviany M. Effective mass diffusivity and water saturation distribution in single- and two-layer PEMFC diffusion medium. Int J Heat Mass Trans 2003;46:4595–611.

[53] Kawamura J, Hattori K, Hongo T, Asayama R, Kuwata N, Hattori T, et al. Microscopic states of water and methanol in Nafion membrane observed by NMR micro imaging. Solid State Ionics 2005;176:2451–6.

[54] Cui S, Liu J, Selvan M, Keffer D, Edwards B, Steele W. A molecular dynamics study of a Nafion polyelectrolyte membrane and the aqueous phase structure for proton transport. J Phys Chem 2007;111:2208–18.

[55] Eisenberg D, Kauzmann W. The Structure and Properties of Water. Oxford University Press, London; 1969.

[56] Kaviany M. Principles of Heat Transfer in Porous Media, 2nd Ed. Srpinger-Verlag, New York; 1999.

[57] Eigen M. Proton transfer, acid-base catalysis, and enzymatic hydrolysis. Angew Chem Int Edit 1964;3(1):1–72.

[58] Zundel G. Hydration structure and intermolecular interaction in polyelectrolytes. Angew Chem Int Edit 1969;8(7):499–509.

[59] Agmon N. The grotthuss mechanism. Chem Phys Lett 1995;244:456–62.

[60] Marx D, Tuckerman M, Hutter J, Parrinello M. The nature of the hydrated excess proton in water. Nature 1999;397:601–4.

[61] Markovitch O, Agmon N. Structure and energetics of the hydronium hydration shells. J Phys Chem A 2007;111:2253–6.

[62] Agmon N. Tetrahedral displacement: The molecular mechanism behind the Debye relaxation in water. J Phys Chem 1996;100:1072–80.

[63] Zhou X, Chen Z, Delgado F, Brenner D, Srivastava R. Atomistic simulation of conduction and diffusion processes in Nafion polymer electrolyte and experimental validation. J Electrochem Soc 2007;154:B82–7.

[64] Stöckelmann E, Aydt E, Hentschke R. Simulation of adsorption isotherms of water on ionic surfaces. J Mol Model 1997;3:347–54.

[65] Freger V. Elastic energy in microscopically phase-separated swollen polymer networks. Polymer 2002;43:71–6.

[66] Kusoglu A, Santare M, Karlsson A. Mechanics-based model for non-affine swelling in perfluorosulfonic acid (PFSA) membranes. Polymer 2009;50:2481–4291.

[67] Kusaka I, Wang ZG, Seinfeld J. Binary nucleation of sulfuric acid-water: Monte carlo simulation. J Chem Phys 1998;108:6829–48.

[68] Hansen JP, McDonald I. Theory of Simple Liquids, 3rd Ed. Academic Press; 2006.

[69] Benjamin K, Singh J, Schultz A, Kofke D. Higher-order virial coefficients of water models. J Phys Chem B 2007;111:11463–73.

[70] Frenkel D, Smit B. Understanding Molecular Simulation: from Algorithms to Applications, 2nd Ed. Academic Press; 2002.

[71] Ryckaert JP, Ciccotti G, Berendsen H. Numerical integration of the cartesian equations of motion of a system with constraints: molecular dynamics of n-alkanes. J Comput Phys 1977;23:327–41.

[72] Berendsen H, Postma J, Gunsteren WV, Dinola A, Haak J. Molecular-dynamics with coupling to an external bath. J Chem Phys 1984;81:3684–90.

[73] Fennell C, Gezelter J. Is the Ewald summation still necessary? pairwise alternatives to the accepted standard for long-range electrostatics. J Chem Phys 2006;124:234104–1–12.

[74] Nicholson D, Parsonage N. Computer simulation and the statistical mechanics of adsorption. Academic Press, London; 1982.

[75] Kaviany M. Heat Transfer Physics. Cambridge University Press, New York; 2008.

NOMENCLATURE

A	cross-section area (m^2)
a_{H_2O}	water activity
D	diffusivity (m^2/s)
d	diameter (m)
h	enthalpy (J/mol)
k_B	Boltzmann constant (J/K)
L	length or domain size
L_t	tortuosity
N	number of fluid particles, water layers, or domains
n	number density (m^{-3})
p	pressure (Pa)
T	temperature (K)

Greek symbols

α	scaling factor
ϵ	water-filled domain volume ratio
δ	thickness (m)
μ	chemical potential (J)
λ_{H_2O}	water content
ρ	density (kg/m^3)
σ_l	surface tension (N/m)
σ_{H^+}	proton conductivity (S/m)
τ	time (s)

Subscripts

ad	adsorption
d	domain
e	electron
eff	effective
f	fluid or water
H_2O	water molecules
H_3O^+	hydronium
lg	liquid-gas phase change, or saturation
p	polymer
SO_3^-	sulfonic acid
wf	water fillable
X, Y, Z	coordinates of x, y, and z

Tables

Table 1: Summary of the SAXS model parameters for Eqs. (2) to (4).

a_{H_2O}	L_Z and L_X , nm	$L_{Z,wf}$, nm in $L_{Z,d}$ = 1 nm	$L_{Z,wf}$, nm in $L_{Z,d}$ = 4 nm	$\Delta n_{e,p}$, Å^{-3}	$\Delta n_{e,ad,H_2O}$, Å^{-3}	$\Delta n_{e,g,H_2O}$, Å^{-3}
0	4.8	1	4	-0.0875	0.02	-0.0045
0.11	5.0	0	3.7	-0.0875	0.02	-0.0045
1	6.0	0	0	-0.18	0.08	-0.1

Table 2: Ratio of domain populations and volumes.

	$L_{Z,d} = 1$ nm	$L_{Z,d} = 4$ nm
$N_{L_{Z,d},i}/N_d$	0.53	0.47
$V_{L_{Z,d},i}/V_{L_Z}$	0.22	0.78

Table 3: Summary of various sulfonic-acid surface site densities in the literature.

$n(SO_3^-)$ nm^{-2}	Comments
1.62	110 sites per 4.65 nm diameter cluster for EW = 1100 g/mol [8]
3.3	$d_{SO_3^-\text{-}SO_3^-}$ = 0.55 nm for T = 20 to 80°C [9]
1.82	the specific surface area of 0.55 nm^2 per site [42]
0.51 to 1.23	$d_{SO_3^-\text{-}SO_3^-}$ = 0.9 to 1.4 nm for $\langle\lambda_{H_2O}\rangle$ = 4 to 15 [36]

Table 4: MD predicted D_{H_2O}, as a function of a_{H_2O} and $\langle\lambda_{H_2O}\rangle$ at T = 300 K for $L_{Z,d}$ = 1 and 4 nm.

a_{H_2O} ($\langle\lambda_{H_2O}\rangle$)	D_{H_2O}, m^2/s at $L_{Z,d}$ = 1 nm	D_{H_2O}, m^2/s at $L_{Z,d}$ = 4 nm
0.05(2.0)	5.70×10^{-10}	5.82×10^{-10}
0.1(3.9)	1.21×10^{-9}	7.64×10^{-10}
0.3(4.8)	1.25×10^{-9}	2.13×10^{-9}
0.5(5.4)	1.27×10^{-9}	2.25×10^{-9}
0.7(6.3)	1.29×10^{-9}	2.45×10^{-9}
0.8(6.9)	1.29×10^{-9}	3.03×10^{-9}
0.9(7.2)	1.30×10^{-9}	3.20×10^{-9}
1.0(13.1)	1.29×10^{-9}	2.80×10^{-9}

Table 5: MD predicted $D_{H_3O^+,D}$, as a function of a_{H_2O} and $\langle\lambda_{H_2O}\rangle$ at $T = 300$ K for $L_{Z,d}$ = 1 and 4 nm.

a_{H_2O} ($\langle\lambda_{H_2O}\rangle$)	$D_{H_3O^+}$, m^2/s at $L_{Z,d} = 1$ nm	$D_{H_3O^+}$, m^2/s at $L_{Z,d} = 4$ nm
0.05(2.0)	3.89×10^{-11}	3.65×10^{-11}
0.1(3.9)	2.25×10^{-10}	9.60×10^{-11}
0.3(4.8)	2.38×10^{-10}	2.62×10^{-10}
0.5(5.4)	3.07×10^{-10}	3.13×10^{-10}
0.7(6.3)	3.58×10^{-10}	3.58×10^{-10}
0.8(6.9)	4.29×10^{-10}	3.69×10^{-10}
0.9(7.2)	4.90×10^{-10}	1.22×10^{-9}
1.0(13.1)	5.25×10^{-10}	1.51×10^{-9}

Figure captions

Fig. 1. (a) The proposed bimodal network model, showing hydration-dependent morphological evolution as a function of water activity (or hydration). (b) The cluster network model [7, 8]. (c) The structural inversion network model [42]. (d) The sandwich-like model [30]. (e) The percolation network model [31]. (f) The parallel, long-channel network model [35].

Fig. 2. (a) Holder for SAXS measurement. (b) Measured, normalized SAXS intensity $I^*(\boldsymbol{q})$ as a function of the scattering wave vector $\boldsymbol{q}$ for Nafion 117 at $a_{\mathrm{H_2O}} = 0$, 0.11, and 1, $T = 298$ K, and $p = 1$ atm. Variations of the predicted intensities at the peaks using Eq. (2) are also shown. (c) The proposed cubical domains **for the polymer matrix, the adsorbed-water layer, and the water-fillable layer.**

Fig. 3. Variations of the MD predicted isosteric heat of adsorption $\Delta h_{lg,ad}$ as a function of the number of adsorbed water layers **at the sulfonic-acid surface densities, $n(\mathrm{SO_3^-}) = 1.75$ and 2.5 nm^{-2}, and the domain sizes, $L_{Z,d} = 1$ and 4 nm**. The adsorbed-water thickness is also shown **at the top x-axis**. The bulk heat of evaporation for MSPC/E water model at $T = 300$ K [48] and the Debye screening length δ_{D} are shown.

Fig. 4. (a) Variations of GCMD-MC results of the adsorbed water at $L_{Z,d} = 1$ nm with respect to the water activity, $a_{\mathrm{H_2O}}$ at $T = 300$ K and $n(\mathrm{SO_3^-})$ = 1.75 nm^{-2}. The predicted results using available adsorption and water filling theories are also shown [6, 10, 27]. (b) Variations of

the adsorbed water at $L_{Z,d} = 4$ nm, $T = 300$ K, and $n(SO_3^-) = 1.5$, 1.75, and 2.5 nm^{-2}. (c) Variations of the predicted water content $\langle \lambda_{H_2O} \rangle$, Eq. (5), as a function of the activity at $T = 300$ K. Available experimental result at $T = 303$ K is also shown [21].

Fig. 5. (a) Variations of water self-diffusion coefficient in Nafion as a function of average water content at 303 K. The experiential results [18] and the available MD results [53, 54], are also shown along with the experimental result for bulk liquid water at $T = 298$ K [55]. (b) Variations of the tortuosity with respect to the water content using the normalized effective diffusivity. The domain **water-filling** regimes are also marked.

Fig. 6. (a) Variations of the predicted proton conductivity, as a function of water content, showing significant increases caused by water filling and bulk-like diffusivity, at $T = 300$ K. The predicted translational-diffusion proton conductivity, and the available experimental results at $T = 303$ K [21] and MD results $T = 298$ K [63] are shown. (b) Predicted domain connectivity with respect to the water content, and comparison with the normalized proton conductivity at $T = 303$ K. The domain **water fillings** are also marked.

Figure1

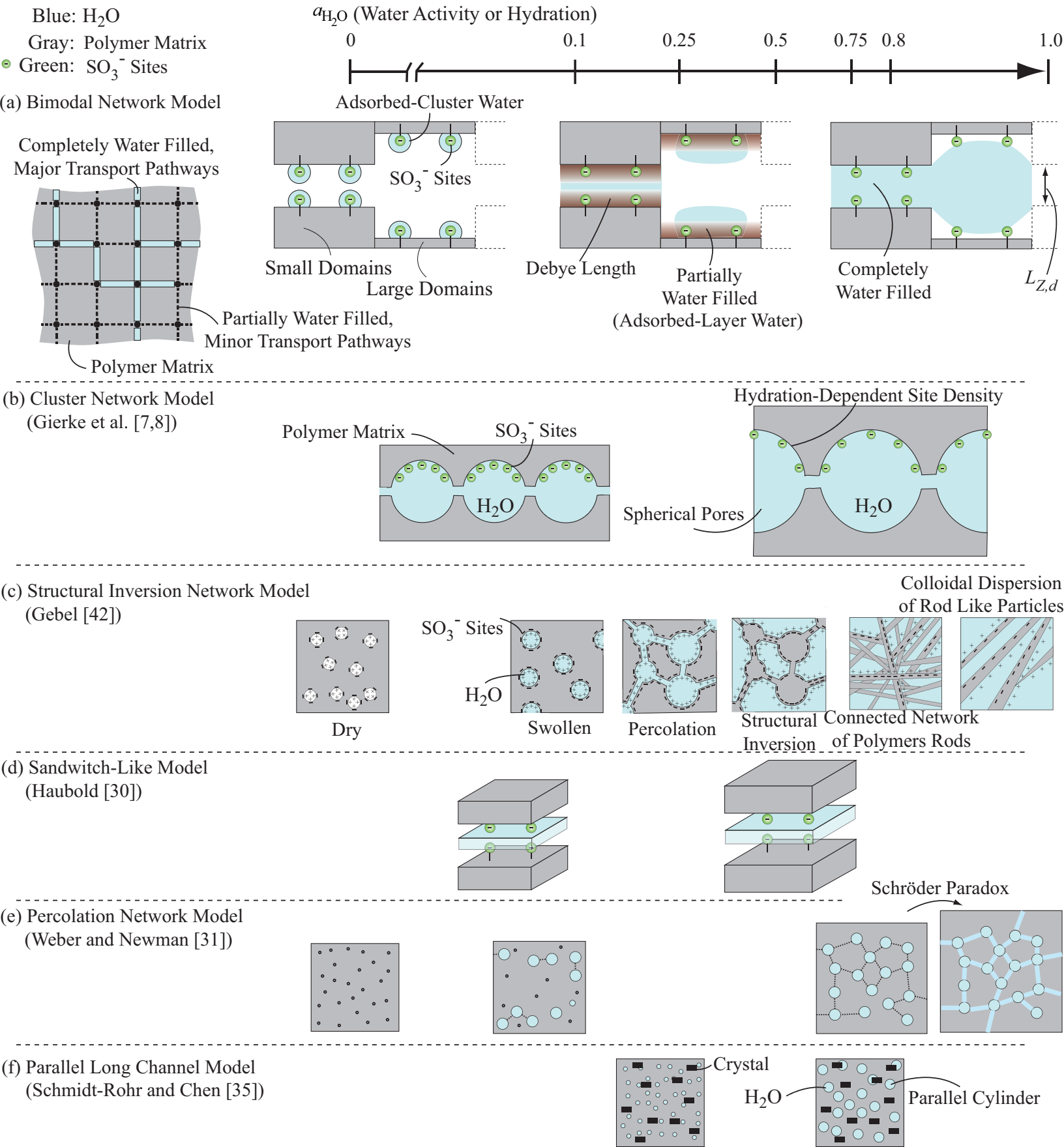
Blue: H_2O
Gray: Polymer Matrix
Green: SO_3^- Sites
a_{H_2O} (Water Activity or Hydration)
0
0.1
0.25
0.5
0.75
0.8
1.0
(a) Bimodal Network Model
Adsorbed-Cluster Water
Completely Water Filled,
Major Transport Pathways
SO_3^- Sites
Small Domains
Large Domains
Debye Length
Partially
Water Filled
(Adsorbed-Layer Water)
Completely
Water Filled
$L_{Z,d}$
Partially Water Filled,
Minor Transport Pathways
Polymer Matrix
(b) Cluster Network Model
(Gierke et al. [7,8])
Polymer Matrix
SO_3^- Sites
H_2O
Hydration-Dependent Site Density
Spherical Pores
H_2O
(c) Structural Inversion Network Model
(Gebel [42])
Colloidal Dispersion
of Rod Like Particles
SO_3^- Sites
H_2O
Dry
Swollen
Percolation
Structural
Inversion
Connected Network
of Polymers Rods
(d) Sandwitch-Like Model
(Haubold [30])
(e) Percolation Network Model
(Weber and Newman [31])
Schröder Paradox
(f) Parallel Long Channel Model
(Schmidt-Rohr and Chen [35])
Crystal
H_2O
Parallel Cylinder

Figure 2

(a) Nafion Holder for SAXS Measurement

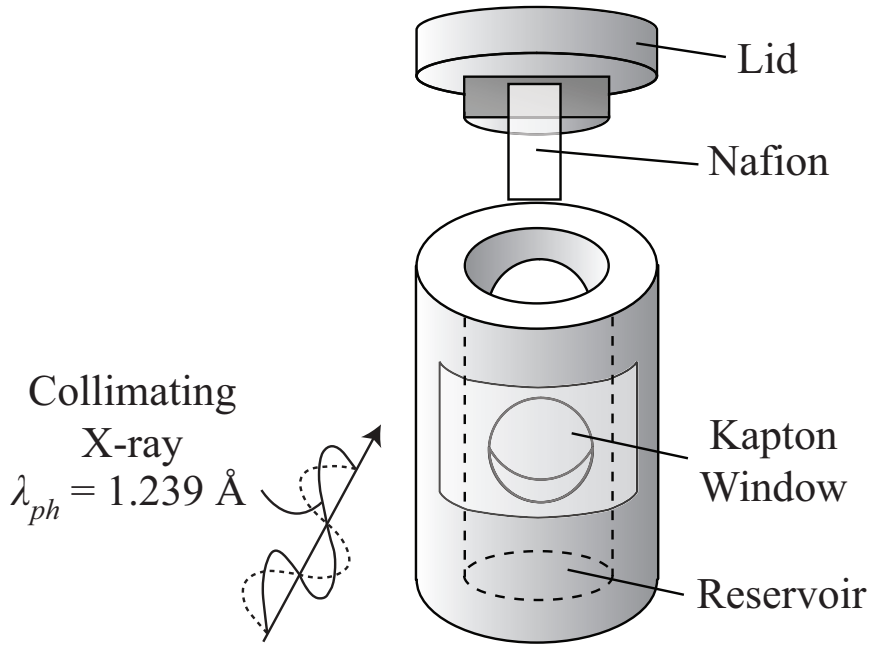

(b) SAXS Measurements and Predictions

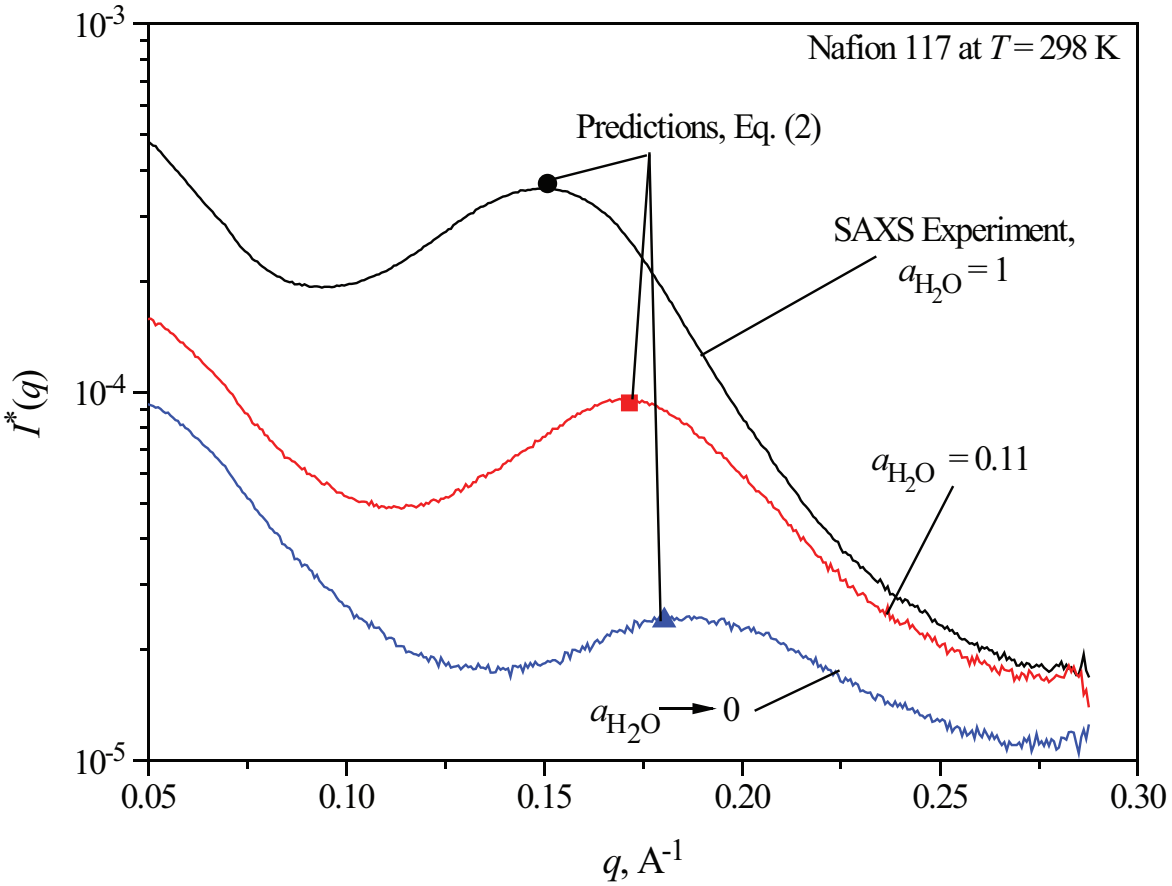

(c) Cubical Domain

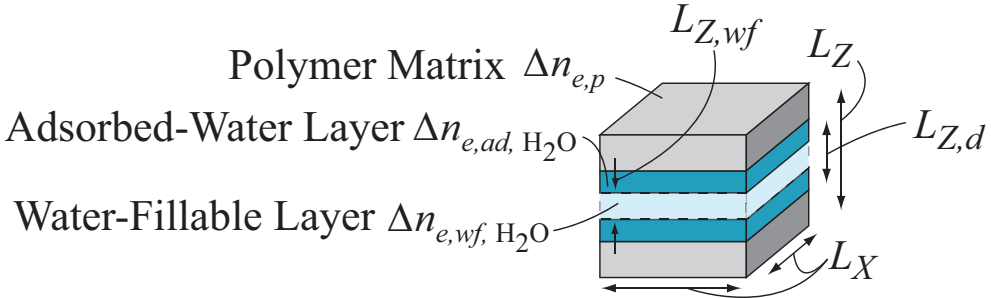

Figure3

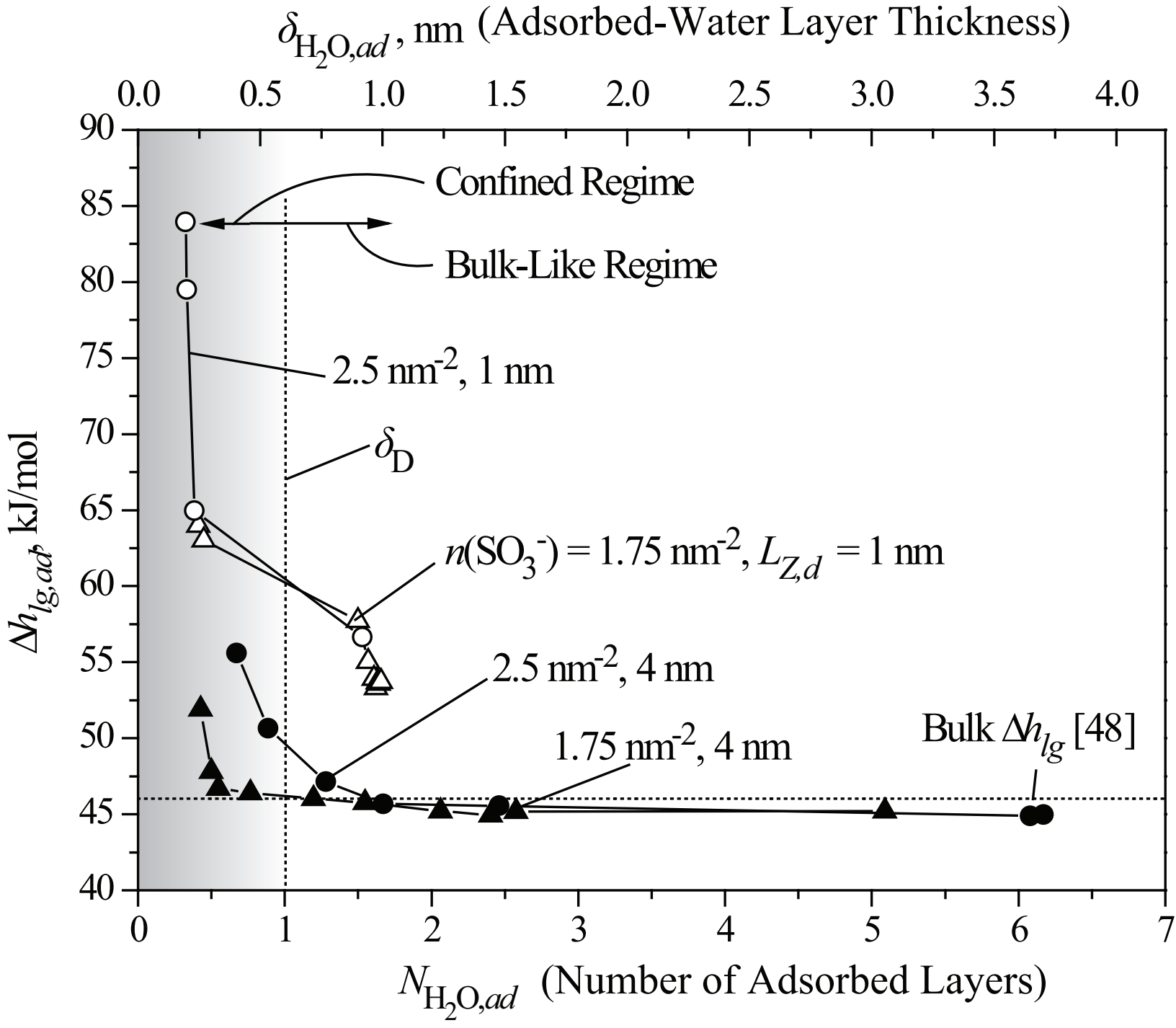
$\delta_{H_2O,ad}$, nm (Adsorbed-Water Layer Thickness)
0.0
0.5
1.0
1.5
2.0
2.5
3.0
3.5
4.0
90
85
80
75
70
65
60
55
50
45
40
Confined Regime
Bulk-Like Regime
2.5 nm^{-2}, 1 nm
δ_D
$n(SO_3^-) = 1.75$ nm^{-2}, $L_{Z,d} = 1$ nm
2.5 nm^{-2}, 4 nm
1.75 nm^{-2}, 4 nm
Bulk Δh_{lg} [48]
$\Delta h_{lg,ad}$, kJ/mol
0
1
2
3
4
5
6
7
$N_{H_2O,ad}$ (Number of Adsorbed Layers)

Figure4

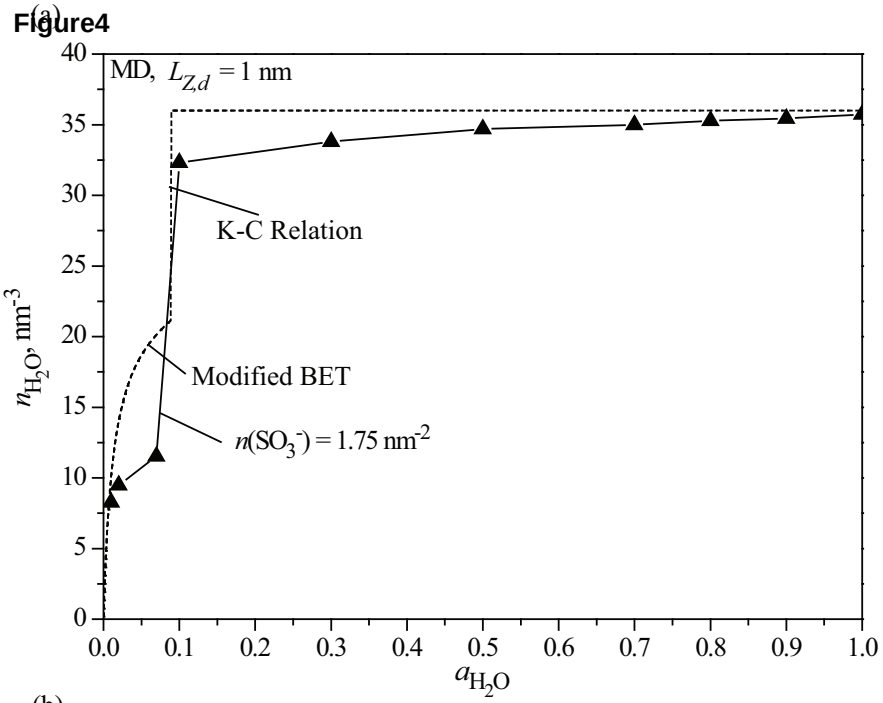
(a)
MD, $L_{Z,d}$ = 1 nm
K-C Relation
Modified BET
$n(SO_3^-)$ = 1.75 nm^{-2}
n_{H_2O}, nm^{-3}
a_{H_2O}

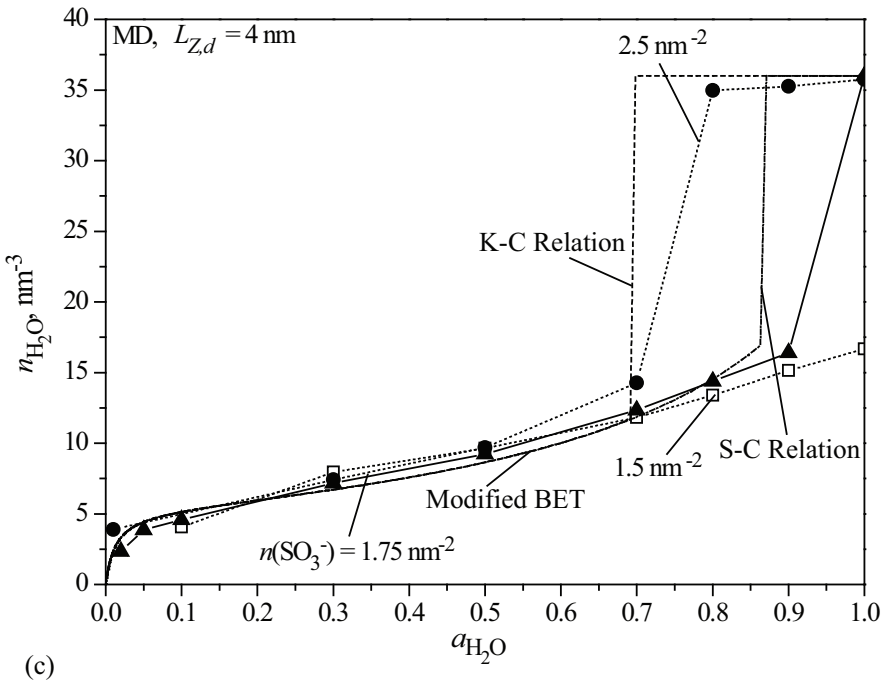
(b)
MD, $L_{Z,d}$ = 4 nm
2.5 nm^{-2}
K-C Relation
1.5 nm^{-2}
S-C Relation
Modified BET
$n(SO_3^-)$ = 1.75 nm^{-2}
n_{H_2O}, nm^{-3}
a_{H_2O}

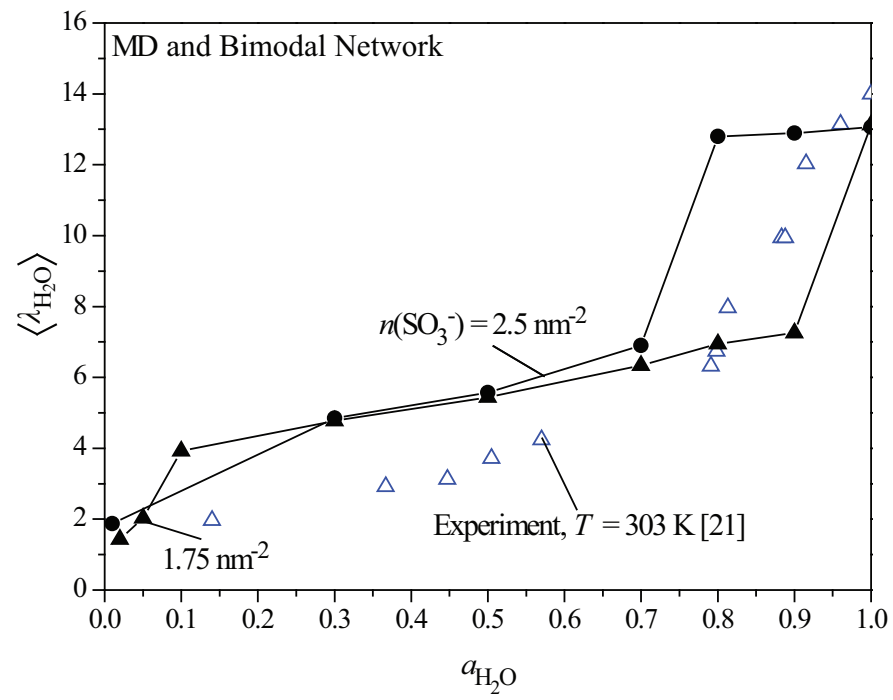
(c)
MD and Bimodal Network
$n(SO_3^-)$ = 2.5 nm^{-2}
Experiment, T = 303 K [21]
1.75 nm^{-2}
$\langle \lambda_{H_2O} \rangle$
a_{H_2O}

Figure5

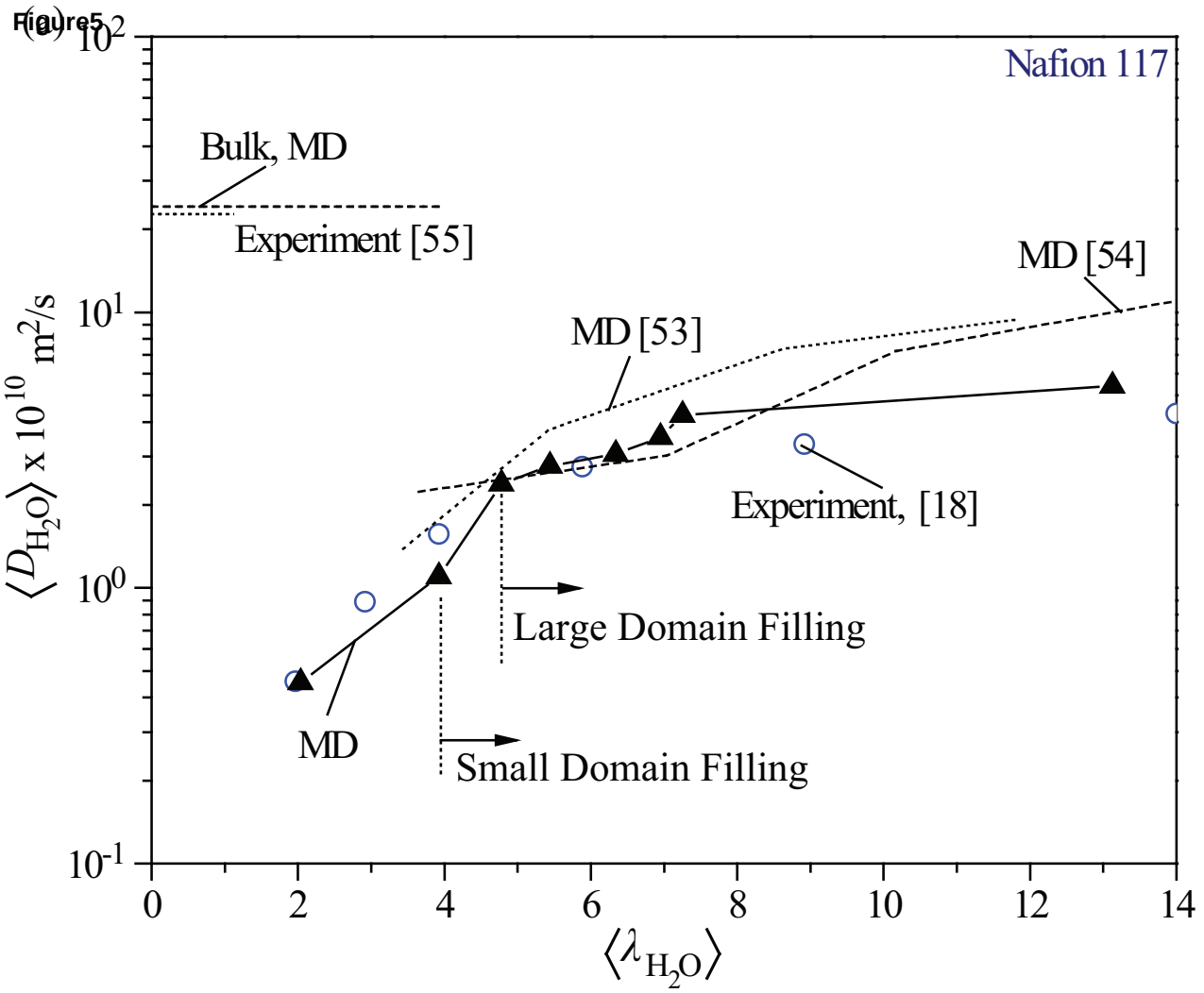
(a)
Nafion 117
Bulk, MD
Experiment [55]
MD [54]
MD [53]
Experiment, [18]
Large Domain Filling
MD
Small Domain Filling
$\langle D_{H_2O} \rangle$ x 10^{10} m^2/s
$\langle \lambda_{H_2O} \rangle$

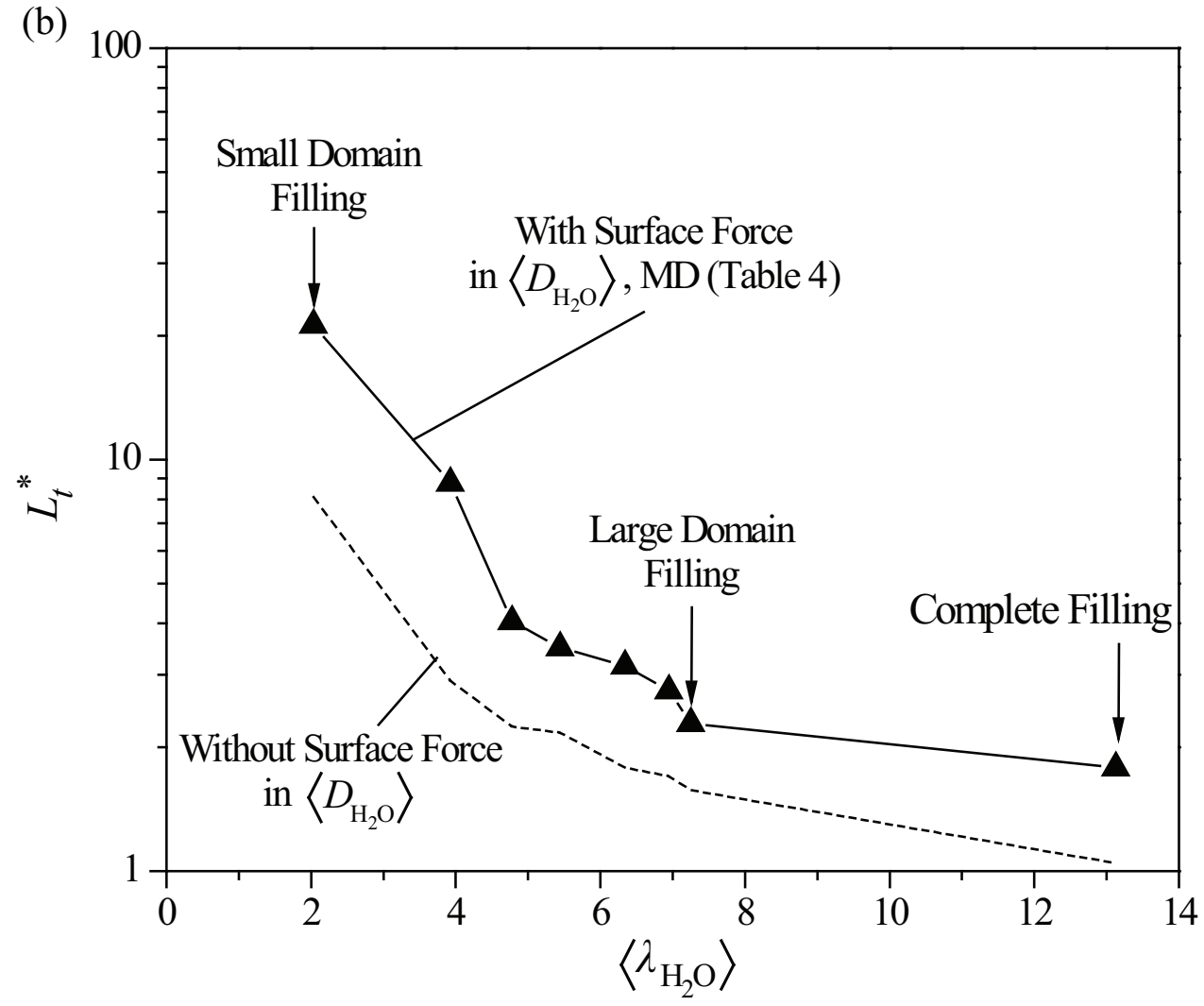
(b)
Small Domain Filling
With Surface Force in $\langle D_{H_2O} \rangle$, MD (Table 4)
Large Domain Filling
Complete Filling
Without Surface Force in $\langle D_{H_2O} \rangle$
L_t^*
$\langle \lambda_{H_2O} \rangle$

Figure6

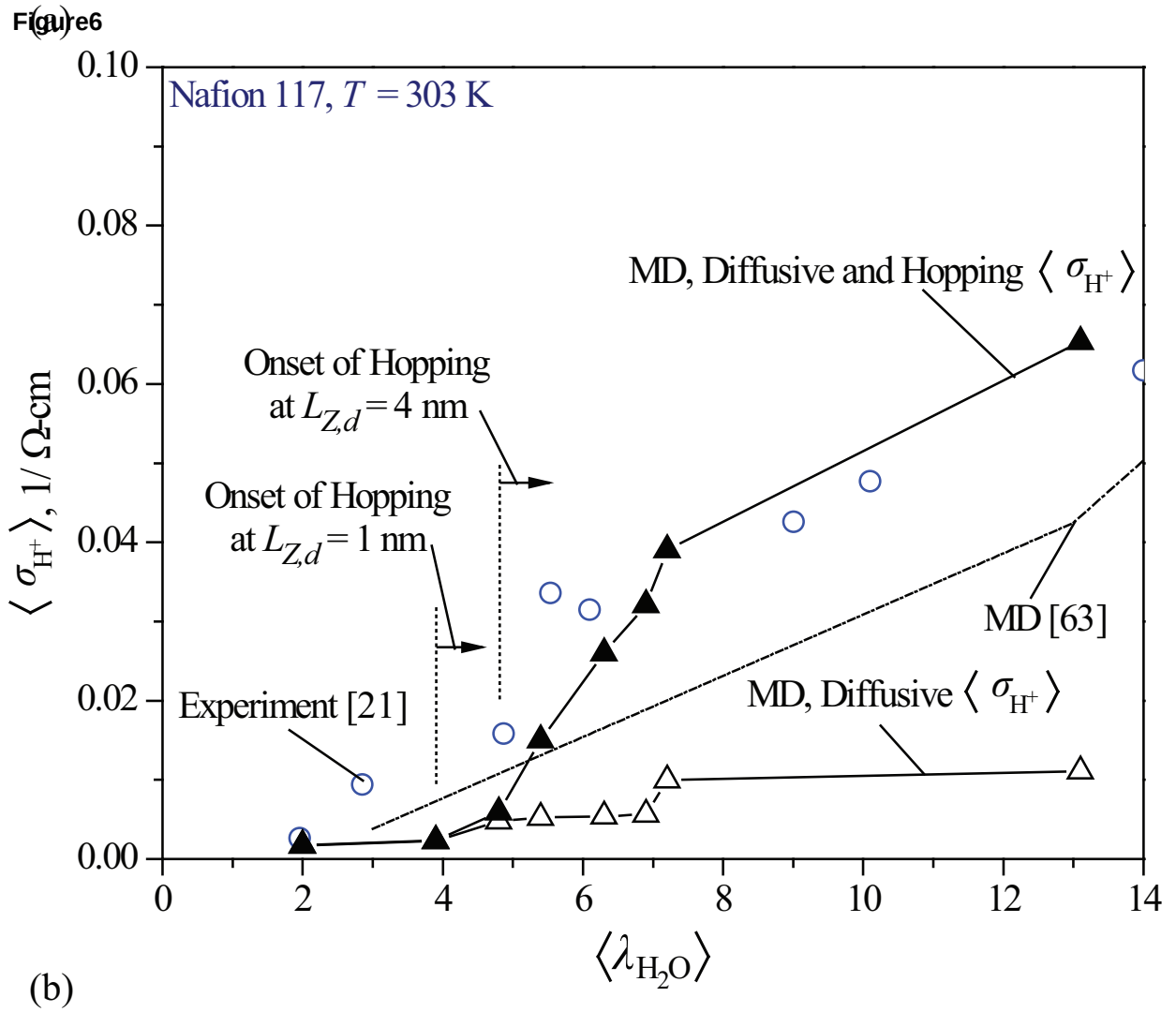
(a)
Nafion 117, T = 303 K
MD, Diffusive and Hopping $\langle \sigma_{H^+} \rangle$
Onset of Hopping at $L_{Z,d}$ = 4 nm
Onset of Hopping at $L_{Z,d}$ = 1 nm
MD [63]
Experiment [21]
MD, Diffusive $\langle \sigma_{H^+} \rangle$
$\langle \sigma_{H^+} \rangle$, 1/ Ω-cm
$\langle \lambda_{H_2O} \rangle$
0.00
0.02
0.04
0.06
0.08
0.10
0
2
4
6
8
10
12
14

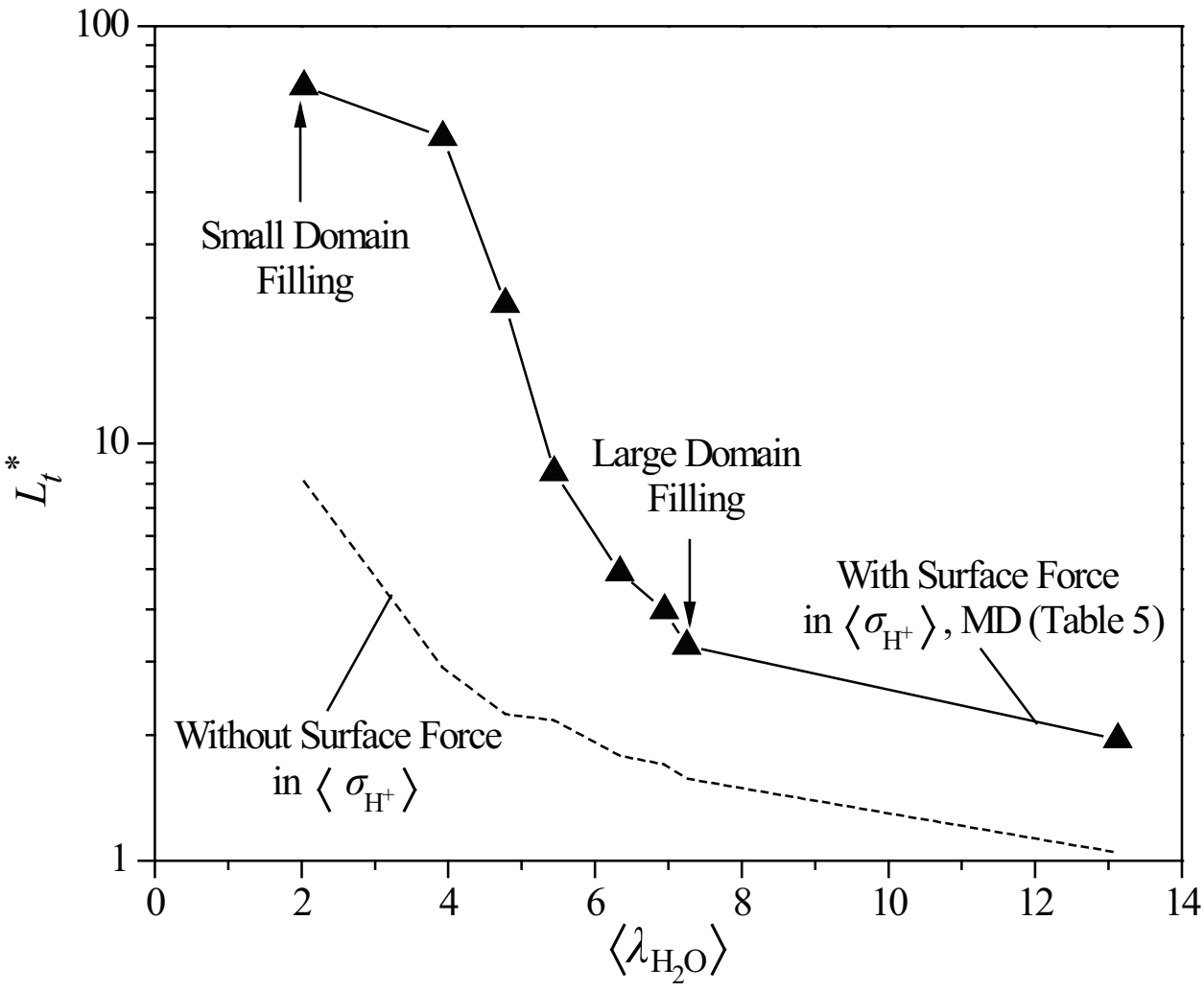
(b)
Small Domain Filling
Large Domain Filling
With Surface Force in $\langle \sigma_{H^+} \rangle$, MD (Table 5)
Without Surface Force in $\langle \sigma_{H^+} \rangle$
L_t^*
$\langle \lambda_{H_2O} \rangle$
1
10
100
0
2
4
6
8
10
12
14